Journal of CO_2 Utilization 32 (2019) 1–10

Contents lists available at ScienceDirect

Journal of CO_2 Utilization

journal homepage: www.elsevier.com/locate/jcou

Low cost and efficient alloy electrocatalysts for CO_2 reduction to formate

Shahid Rasul*, Adrien Pugnant, Hang Xiang, Jean-Marie Fontmorin, Eileen H. Yu*

School of Engineering, Newcastle University, Newcastle Upon Tyne, United Kingdom

ARTICLE INFO

Keywords:
Electrocatalysts
CO_2 reduction
Alloy
Formate
Metal/metal oxide

ABSTRACT

Oxide-derived (OD) Sn and Sn − Pb − Sb composite electrocatalysts were prepared by electrochemical oxidation treatment at various potentials for electrochemical reduction of CO_2 (eCO_2R) for formate ($HCOO^-$) production. The morphology, elemental mapping, phase identification, surface characteristics and electrochemical performance of the electrocatalysts were probed systematically. The surface of OD-Sn and OD-Sn-Pb-Sb shows polycrystalline electrodes with porous morphology and XPS results confirm the formation of composite metal/metal oxide surface related to Sn, Pb and Sb. The EDX mapping analysis shows two distant regions of Pb and Sn rich areas in the alloy. The electrochemical results demonstrate that pristine Sn electrodes show higher CO_2 Faradaic Efficiency (FE) to formate compared to pristine Sn-Pb-Sb alloy electrode (80% vs. 66%) at −1.4 V vs. RHE. Upon oxidation treatment of pristine Sn at 4 V, the FE_{HCOO-} improves to 84% at the expense of decreased current density. On the contrary, upon oxidation treatment of Sn-Pb-Sb alloy at 5 V, the FE_{HCOO-} improved remarkably from 68% to 91% without any reduction in current density. The improved eCO_2R performance of OD-Sn and OD-Sn-Pb-Sb electrodes relative to their pristine electrodes could be attributed to the presence of composite metal/metal oxide structure which leads to local geometric and electronic structural changes.

1. Introduction

The continuous increase of CO_2 in the atmosphere is a major environmental sustainability challenge asking scientists to develop low carbon fuel technologies using renewable sources [1]. Electrochemical CO_2 reduction (eCO_2R) is a promising way for the direct production of renewable fuels and feedstock materials such as CO [2], formic acid (HCOOH) [3] for chemical industries. However, poor selectivity, low activity, energy inefficiency and instability of the current CO_2 reduction electrocatalysts makes the process economically impractical [4]. Therefore, much fundamental understanding is required at the molecular/atomic levels to improve the overall energy efficiency and product selectivity [5]. The critical reason for the ineffectiveness of the metal electrocatalysts for aqueous CO_2 reduction is H_2 generation due to competitive proton (H^+)/ water (H_2O) reduction [6].

P-block based electrocatalysts are among the potential candidates for CO_2 reduction due to their high hydrogen evolution reaction (HER) overpotentials [7]. Tin (Sn) [8–13], Lead (Pb) [14] and Indium (In) [15,16] metal electrodes are well known electrocatalysts for CO_2 reduction to formate but little work has been done to engineer the surface structuring. Especially, Sn metal has been studied extensively as an electrocatalyst for CO_2 reduction due to its high overpotential for H_2 evolution and high selectivity for formate ($HCOO^-$) in the aqueous electrolytes. However, due to low stability of $CO_2^{\cdot -}$ intermediate high overpotentials of at least −1.0 V vs. RHE are required for CO_2 reduction reaction to achieve conversion current up to 5.0 mA cm^{-2}. To overcome the challenge of high overpotentials, Kanan et al. reported [8] that the presence of metastable oxides on the surface of metal catalyst accelerates the CO_2 conversion process by stabilizing the $CO_2^{\cdot -}$ intermediate on the nano-interface compared to pure metallic interfaces. The authors modified the metallic surface of polycrystalline metals (Cu, Au, Sn) to metal oxides by various oxidative treatments and tested the materials for CO_2 conversion reaction. [8,17–21]. The corresponding eCO_2R results confirmed the effectiveness of these modifications.

Until now most of the reported electrocatalysts for eCO_2R are of analytical grade and commercial grade electrocatalysts have rarely been reported [10,22–24]. Considering the practical aspects of eCO_2R, the CO_2 gas most probably will be collected from industrial flue gases demanding that the electrocatalysts must be robust towards impurities. Therefore, there is a dire need to analyze the commercially available electrocatalysts for CO_2 reduction which are low cost and robust during the eCO_2R [25,26].

In this study, we report for the first time a commercially available Sn-Pb-Sb alloy electrocatalyst (widely used as low melting point solder) for CO_2 reduction reaction to produce formate with high efficiency. Sn-Pb-Sb alloy electrocatalyst was selected due to its low cost and

* Corresponding authors.
E-mail addresses: Shahid.rasul@ncl.ac.uk (S. Rasul), eileen.yu@ncl.ac.uk (E.H. Yu).

https://doi.org/10.1016/j.jcou.2019.03.016
Received 18 May 2018; Received in revised form 18 March 2019; Accepted 20 March 2019

robustness. Since the activity of a catalyst depends upon the electrode surface (morphology, surface bound species and composition) [8,27–29], further modifications of Sn and Sn-Pb-Sb alloy catalysts for eCO_2R were carried out. Sn-Pb-Sb alloy catalysts were oxidized electrochemically to produce oxide-derived (OD) electrocatalysts. We hypothesized that metastable metal oxides (MO_x) on the Sn-Pb-Sb surface would not only stabilize the $CO_2^{\cdot -}$ but would prefer C coordination of $CO_2^{\cdot -}$ with evolved grain boundaries [30]. Thus, the Sn and Sn-Pb-Sb electrodes were prepared and characterized by various characterization techniques and tested for eCO_2R reaction.

2. Experimental

2.1. Preparation of oxide derived electrocatalysts

Sn (99.95%, 0.125 mm thick) from Advent Research Materials, UK and a commercial Sn-Pb-Sb alloy foil (Sn 60%, Pb 39%, Sb 1%), were obtained from Goodfellow Cambridge Ltd. For fabrication of oxide derived electrodes, Sn and Sn-Pb-Sb alloy were employed as working electrodes at different cell voltages (4 V, 5 V, 7 V and 9 V) for 30 min and Pt wire was used as a counter electrode. The oxide-derived electrodes were then denoted as OD-Sn-XV where X is the applied voltage. The working and counter electrodes were separated by a Cation Ion Exchange Membrane (CEM) (fumapem® F-950, FumaTech, Germany) and 0.3 M oxalic acid was used as an electrolyte in both of the electrode chambers.

2.2. Electrochemical reduction of CO_2 to formate and characterization of catalysts

For electrochemical reduction of CO_2, a custom made two compartment electrochemical cell separated by a CEM (fumapem® F-950, FumaTech, Germany) was employed. Electrochemical tests were conducted by an AutoLab potentiostat (PGSTAT204, Metrohm, Switzerland). Three electrodes were used to monitor the current-potential response of the working electrode. Sn metal and Sn-Pb-Sb alloy substrates and Pt wire were used as working and counter electrodes respectively. Ag/AgCl (in 3 M NaCl, 0.208 vs SHE) was employed as a reference electrode. All the applied potentials were converted to reversible hydrogen electrode (RHE) afterwards. Reversible Hydrogen Electrode (RHE) was calculated using E (vs. RHE) = E (vs. Ag/AgCl) + 0.208 V + 0.0591 V*pH). All potentials are clearly marked. 0.1 M $KHCO_3$ (pH = 8.4) (Alfa Aesar, 99%) was used as an electrolyte for eCO_2R studies. The electrolyte was then saturated with CO_2 with gas bubbling for 1 h prior to the eCO_2R reaction. The final pH of the electrolyte was 6.8 after one hour of CO_2 gas bubbling. A continuous flow of CO_2 was maintained by bubbling the CO_2 in the electrolyte during eCO_2R anticipating large current densities for CO_2 reduction products to minimize the mass transport limitations. The flow rate of CO_2 was 20 ml min^{-1} to ensure sufficient CO_2 transport to the surface while preventing interference from gas bubbles striking the surface.

Cyclic voltammetry (CV) and choronoamperometric analysis (CA) were employed. CVs were carried out at 50 mV s^{-1} scan rate between − 1.5 to + 0.1 V vs. RHE for three cycles. CA was conducted by holding potential of − 0.4 to − 1.4 V vs. RHE at working electrode for 60 min and then gas/liquid samples were collected for product analysis. The electrochemical impedance spectroscopy (EIS) data were obtained in a frequency range of 100 kHz - 0.01 Hz with 10 mV amplitude. Real Z′ and imaginary Z″ parts are extracted from the measurements and expressed in Nyquist representation. The impedance spectra were analyzed using Nova 2.1.2 software.

2.3. Product identification

For eCO_2R products analysis, an offline Ion Chromatography (IC) (ECoIC, Metrohm, Switzerland) and gas chromatography (GC) (Tracera, Shimadzu) equipped with BID detector were employed. For analysis of gaseous products, packed shincarbon column (Restek) was used. To quantify the formate, IC was equipped with Metrosep Organic Acids-100/7.8 column. Analytical methods were developed and optimized to identify formate by IC. Before analysis the IC instrument was calibrated by spiking up with formic acid and a linear calibration curve was obtained. GC was calibrated using mixture of various gases including CO and H_2 and linear calibration curves were established. The minimum detection limit for liquid and gas products were 1 ppm and 50 ppm respectively.

2.4. Material characterization of electrocatalysts

Field Emission Scanning Electron Microscopy (XL30 ESEM-FEG, Philips) and Energy Dispersive X-ray (EDX) spectroscopy were used to investigate size, and morphology and metal composition of the electrodes. X-ray diffraction (XRD) patterns were recorded using a Philips X-ray diffractometer PW 1730 diffractometer equipped with a Cu X-ray tube (Cu–Kα; λ = 0.154 nm) operated at 40 kV and 40 mA. X-ray photoelectron spectroscopy (XPS) was performed on a Thermo Fisher Scientific K-alpha$^+$ spectrometer. Samples were analysed using a micro-focused monochromatic Al x-ray source (72 W) over an area of approximately 400 µm. Data was recorded at pass energies of 150 eV for survey scans and 40 eV for high resolution scan with 1 eV and 0.1 eV step sizes respectively. Charge neutralisation of the sample was achieved using a combination of both low energy electrons and argon ions. Data analysis was performed in CasaXPS using a Shirley type background and Scofield cross sections, with an energy dependence of − 0.6.

3. Results and discussion

3.1. eCO_2R performance of Sn and OD-Sn electrocatalysts

To assess the eCO_2R performance of the electrodes for formate production choronoamperometric analysis was carried out and the total current density (j) and FE are plotted in Fig. 1 (a) for Sn, (b) OD-Sn-4 V and (c) OD-Sn-5 V. The results show that current density increases (electrocatalytic activity) with increasing the CO_2 reduction potentials (overpotentials) in Sn, OD-Sn-4 V and OD-Sn-5 V. However, with increasing the oxidation potential treatment, the overall current density is reduced from 11 to 5 mA cm^{-2} at Sn and OD-Sn-5 V respectively. The drop in more than half of current density in OD-Sn-5 V could be ascribed to the insulating nature of SnO_2 formed at 5 V oxidation treatment. On the contrary, the selectivity of eCO_2R to formic acid improves upon oxidation treatment of Sn which peaks at the 4 V oxidized electrode at around 84% at − 1.4 V vs. RHE. Upon further oxidation at 5 V, the current density and FE both decrease rendering 4 V (optimum oxide thickness) electrode the best on in this series of samples at all the applied potentials. The objective is to increase the performance of CO_2 reduction, preferably at low overpotential which have been achieved with OD-Sn-4 V cathode because FE has risen by 26% at − 1.0 V and 18% at − 0.8 V vs RHE compared to pristine Sn. The OD-Sn-4 V appears to have a similar current density trend to Sn but higher FE owing to the increased selectivity to formate of the electrode. In addition to OD-Sn-4 V and 5 V, OD-Sn-7 V and 9 V were also prepared which resulted in very thick SnO_2 layers (Fig. SI 1). OD-Sn-7 V and 9 V were employed for eCO_2R. However, due to their thick insulating SnO_2 layers, chronoamperometric analysis could not be carried out.

Based on electrochemical performance results, OD-Sn-4 V electrode was selected for further characterization and CO_2 reduction studies. Fig. 2 shows a representative CV in the potential window of − 1.5 to + 0.1 V vs. RHE of a pristine and oxidized Sn electrode at 4 V. In the case of Sn, the anodic scan displays two anodic peaks (labelled as I and II) in the − 0.1 V and 0.1 V range. Peak I has been assigned to the oxidation of Sn to Sn^{2+}, while peak II has been ascribed to the

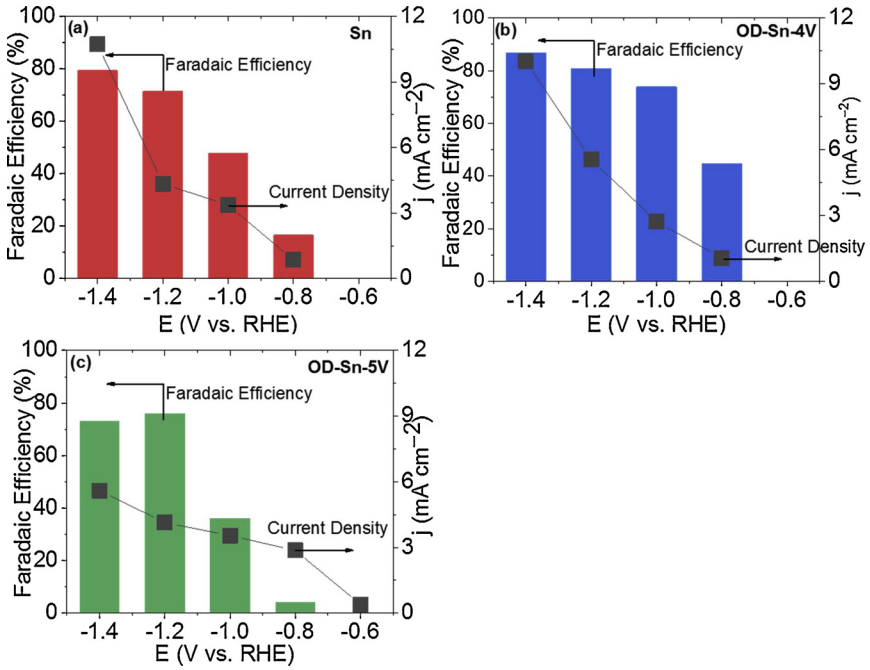

Fig. 1. (a–c) Total geometric current density and Faradaic efficiency profiles of Sn and Sn oxidized electrodes during choronoamperometric analysis at various potentials in CO_2 saturated 0.1 M $KHCO_3$ electrolyte.

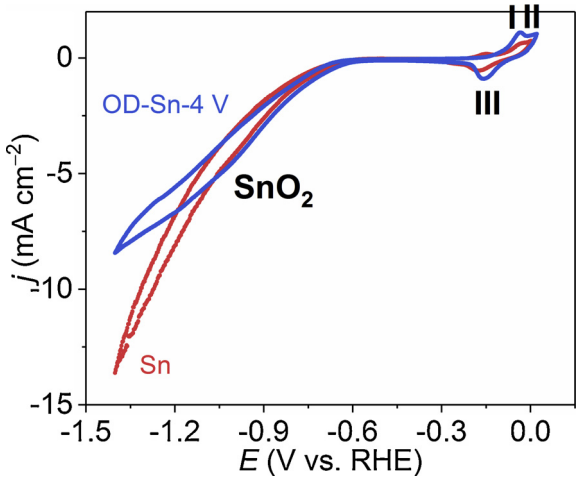

Fig. 2. A representative CV profile of Sn and OD-Sn-4V in CO_2 saturated 0.1 M $KHCO_3$ at the scan rate of 50 mV s^{-1}.

generation of Sn(IV) species to produce a passive $Sn(OH)_4$ or SnO_2 [31,32]. On the reverse scan, the peak at around −0.2 V corresponds to Sn (II) reduction to Sn (0). In the case of Sn electrodes oxidised at 4 V, there is an additional broad cathodic peak at around −0.9 V which arises from the reduction of SnO_2 layer confirming the formation of SnO_2 layer [31,32] upon oxidation at 4 V. This peak becomes more evident in case of OD-Sn-7 V as shown in CV profile of OD-Sn-7 V in Fig SI 1. It is important to note that due to formation of oxide layer at the surface of OD-Sn-4 V, the electrocatalytic current density beyond −0.9 V vs. RHE reduces which was observed in choronoamperometric results of eCO_2R as well (Fig. 1). These results, thus suggest that OD-Sn electrodes may have improved the selectively of formate production but the improved selectivity is obtained at the expense of reduced current density (electrocatalytic activity).

To investigate the surface morphology of Sn and OD-Sn-4 V electrode, SEM analysis was carried out as shown in Fig. 3. The surface morphology of Sn electrode shows a flat Sn sheet with relatively smooth surface. On the contrary, the SEM image of OD-Sn-4 V shows that the surface morphology was transformed completely from flat structure to rough and porous structure. The morphological change of OD-Sn-4 V in SEM image also points that the Sn metal was successfully oxidized as evidenced by CV profile (Fig. 2) as well. The change in surface roughness and morphology of OD-Sn-4 V may have increased the surface area but due to the insulating character of SnO_2, the increased surface area was rendered as inactive as shown in CV and chronoamperometric analysis results (Fig. 1 and 2).

XRD analysis was carried out to analyse the phase identification of the Sn electrodes before oxidation, after oxidation and after eCO_2R studies as shown in Fig. 4. The XRD profiles of pristine Sn and OD-Sn-4 V show that both electrodes are polycrystalline Sn materials with a highest intensity peak (211) at 2θ of 45.1° (JCPDS#04-00−2820). However, a major difference is observed in the pristine Sn and OD-Sn-4 V after eCO_2R electrode where the intensity of (112) peak at 63° decreases compared to the (112) peak of OD-Sn-4 V. The change in the intensity of the Sn peaks shows that the electrodes undergo structural changes during the eCO_2R reaction as confirmed by SEM analysis as well. However, the XRD analysis, thus suggests that no bulk crystal phase change occurred in response to oxidation treatment of Sn electrode.

3.2. *eCO_2R performance of Sn-Pb-Sb and OD-Sn-Pb-Sb electrocatalysts*

To investigate the oxidation/reduction and CO_2 reduction behaviour of the Sn-Pb-Sb alloy cyclic voltammetry was carried out in the −1.5 to + 0.1 V vs. RHE potential range for a pristine Sn-Pb-Sb alloy and OD-Sn-Pb-Sb-5 V electrode in N_2 and CO_2 saturated 0.1 M $KHCO_3$ (Fig. 5). In the case of pristine alloy, relatively smaller oxidation and reduction redox peaks at -0.05 and -0.20 V were observed in CO_2 atmosphere arising from surface oxidation and reduction. However, in the case of OD-Sn-Pb-Sb when the electrode is tested N_2 conditions, the redox couple is observed at −0.1 and −0.35 V. When the OD-Sn-Pb-Sb is tested under CO_2 conditions, the 1st cathodic cycle displays three distinct redox peaks in the 0.05 V, −0.3 and −0.5 V range confirming the successful oxidation of the alloy at 5 V. These redox peaks could be attributed to the oxidation of multi-metals (Sn, Pb, Sb). This is

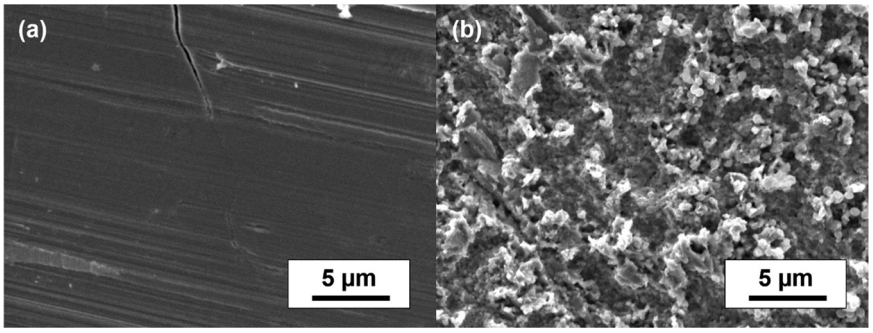

Fig. 3. SEM images of (a) Sn electrode (b) OD-Sn-4V.

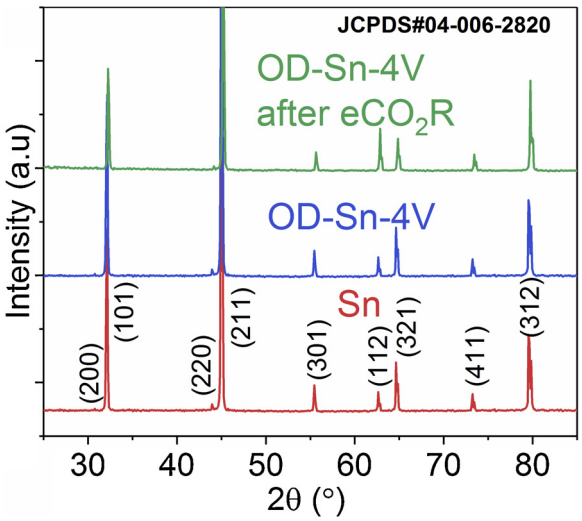

Fig. 4. XRD profile of pristine Sn, OD-Sn-4V and OD-Sn-4V after eCO_2R.

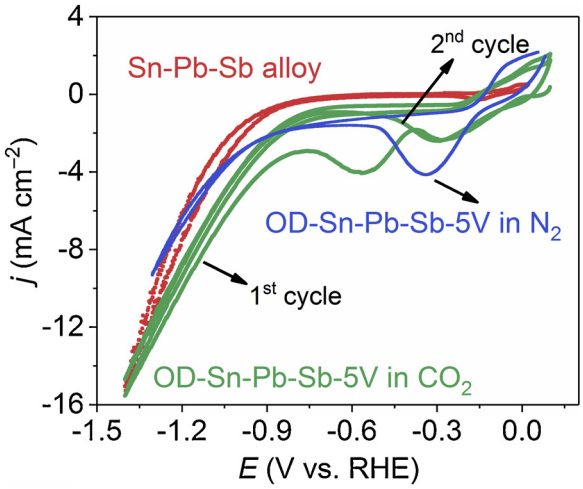

Fig. 5. A representative CV profile of Sn-Pb-Sb and OD-Sn-Pb-Sb-5V alloy at 50 mV s^{-1} in CO_2 saturated 0.1 M $KHCO_3$.

interesting to note that when OD-Sn-Pb-Sb electrode is tested under CO_2 conditions, the current density increases upto ~ −16 $mAcm^{-2}$ at −1.4 V and the onset potential shifts towards positive potentials (−0.65 V). In comparison to the electrode when tested under N_2 the current density is ~ −8 $mAcm^{-2}$ at −1.4 V while the onset potential is −0.9 V confirming the enhanced eCO_2R activity of OD-Sn-Pb-Sb electrocatalyst. Similarly, CV analysis for pristine Sn-Pb-Sb control sample was carried out also under CO_2 and N_2 conditions as shown in Fig. SI 3. The CV profiles clearly show that electrocatalytic activity of Sn-Pb-Sb is enhanced under CO_2 atmosphere.

Pristine Sn-Pb-Sb and OD-Sn-Pb-Sb electrodes were tested for electrochemical eCO_2R and the total current density and FE results are shown in Fig. 6 (a–f). The maximum current density for pristine Sn-Pb-Sb and OD-Sn-Pb-S[7] V alloy is about 8 and 10 mA cm^{-2} at −1.4 V vs. RHE respectively. The overall comparison of eCO_2R activity (current density) of pristine and OD alloy shows that the current density values remain in the range of ~ 7–10 mA cm^{-2} for both Sn-Pb-Sb and OD-Sn-Pb-Sb electrodes. The retaining of high current density in Sn-Pb-Sb alloy even after oxidation treatment is a promising feature of these electrocatalyst for CO_2 reduction in contrast to the OD-Sn where current density decreases sharply with oxidation treatment of the electrodes.

As expected, the current density increases with increasing the reduction potentials in all of the alloy electrodes irrespective of untreated and oxidized electrodes. The FE results show that selectivity of eCO_2R towards formate increases upon oxidation treatment which peaks at OD-Sn-Pb-Sb-5 V and 7 V electrode at about 91% at −1.4 V vs. RHE. Notably, the higher selectivity trend of eCO_2R to formate (FE ~ 60%) is observed at lower reduction potentials (−1.0 V vs. RHE) as well in both OD-Sn-Pb-Sb-5 V and 7 V electrodes compared to pristine Sn-Pb-Sb electrode (FE ~ 35%) at same potentials. These results clearly suggest that oxidation treatment of Sn-Pb-Sb alloy improves the eCO_2R to formate at a range of applied potentials from −0.8 to −1.4 V vs. RHE. However, upon further oxidation of the alloy at 9 V, the FE to formate production decreases to 75% at −1.4 V vs. RHE. The possible reason for decrease in eCO_2R activity of OD-Sn-Pb-Sb-9 V electrode could be the formation of a dense and thick layer of oxide which may hinder the charge transfer reaction to CO_2. These results thus render OD-Sn-Pb-Sb-5 V (optimum oxide thickness) electrode as the best electrode in this series of alloy electrode samples. The better performance of the OD alloy could be attributed to the oxidation of electrocatalysts which permits to alter the surface geometry/morphology which contributes to increased conversion of CO_2 and brings a noticeable difference between FE of oxidized and non-oxidized electrodes.

Based on the eCO_2R performance of alloy electrode results, pristine alloy electrode and electrodes prepared by oxidizing Sn-Pb-Sb at 5 V for 30 min were selected for further characterization and eCO_2R studies. It is interesting to note that in OD-Sn-Pb-Sn electrodes, with increasing the oxidation potential treatment, overall current density remains high which is contrary to oxidation treated Sn electrodes (Figs. 1 and 6). This could be attributed to the presence of Sb in the alloy electrode which improves the electronic conductivity of SnO_2 [33]. To confirm the impact of Sb on the electrode conductivity, impedance spectroscopy on OD-Sn-Pb-Sb-5 V was performed at open circuit potential. Fig. 7 (a) demonstrates the comparative impedance spectra in Nyquist representation for pristine Sn-Pb-Sb and OD-Sn-Pb-Sb-5 V before and after eCO_2R. The enlarged dataset is presented in Fig. 7 (b). An equivalent electrical circuit was fitted using a Randles circuit that consisted of an active electrolyte resistance (R_S) in series with the parallel combination of the double-layer capacitance (C_{dl}) and a charge transfer resistance

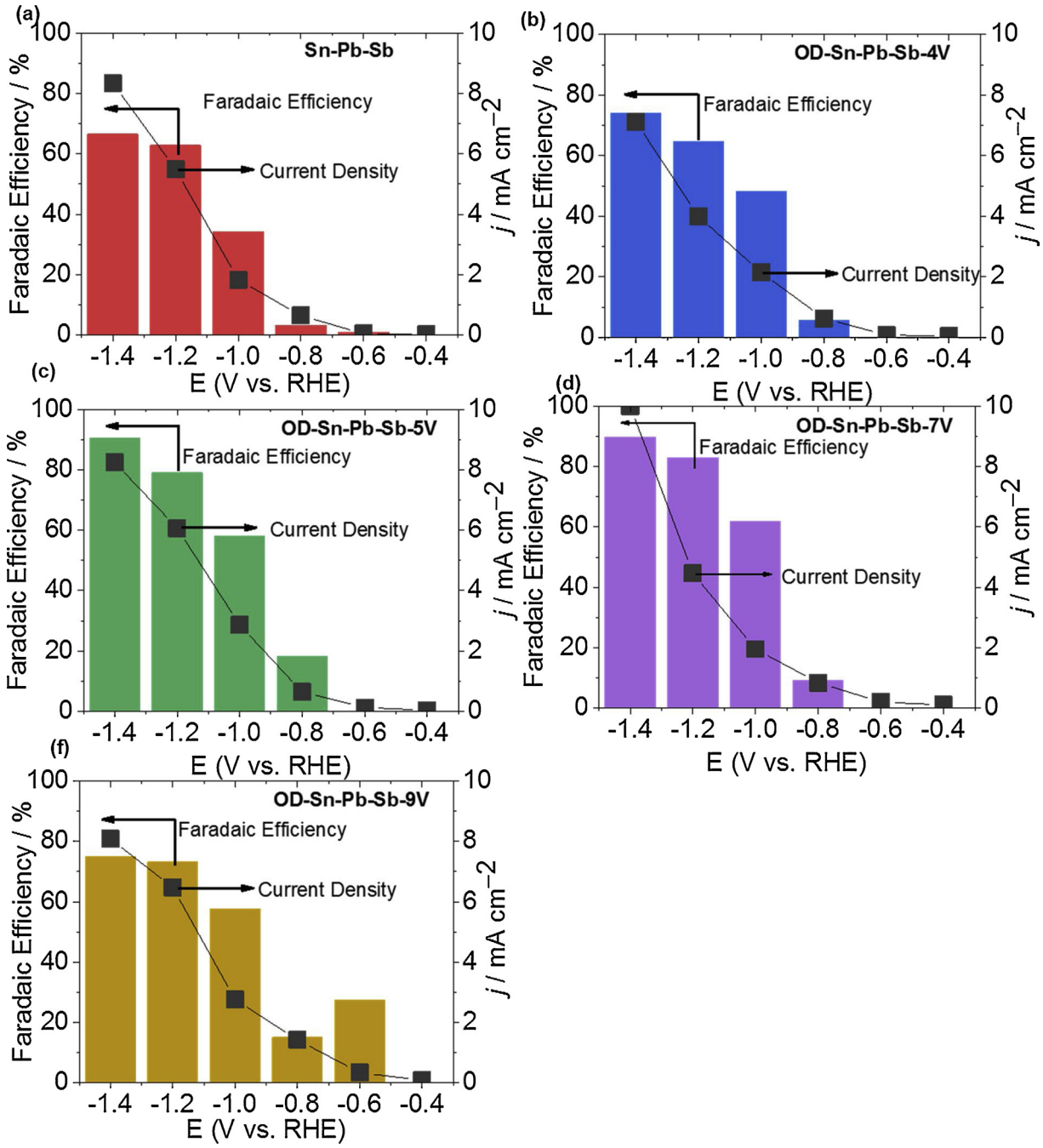

Fig. 6. (a–f) Total current density and FE obtained vs applied Potential during CA in CO_2-saturated 0.1 M $KHCO_3$ electrolyte.

(R_{CT}) in the reaction. The comparison between EIS spectra of pristine Sn-Pb-Sb and OD-Sn-Pb-Sb before eCO_2R shows that the charge transfer resistance in pristine Sn-Pb-Sb is an order of magnitude higher than OD-Sn-Pb-Sb-5 V in identical conditions. This result implies that the conductivity of the alloy improves after oxidation treatment which ultimately improves the charge transfer to CO_2. Especially, the charge transfer resistance on OD-Sn-Pb-Sb is further reduced when the electrode is employed for eCO_2R reaction for several hours. This behaviour suggests that the electrode surface is not only reducing the CO_2 during the reaction but also going through structural reorganisation.

To further investigate the conductivity effect on eCO_2R, the comparative EIS spectra of OD-Sn-4 V and OD-Sn-Pb-Sb-5 V at open circuit potential are shown in Fig. 8 (a). The enlarged dataset is presented in Fig. 8 (b). The impedance spectra clearly shows that OD-Sn has higher charge transfer resistance (30,665 Ω) than OD-Sn-Pb-Sb-5 V electrode (603 Ω). The EIS results confirm that presence of a small amount of Sb (1 wt%) improved the conductivity of the alloy tremendously which also enhances eCO_2R activity.

XRD analysis was carried out to analyse the phase identification of the Sn-Pb-Sb alloy before oxidation, after oxidation and after eCO_2R studies as shown in Fig. 9. The XRD profiles of pristine Sn-Pb-Sb and OD-Sn-Pb-Sb show that both electrodes are polycrystalline materials with a mixture of Sn and Pb rich phases. The highest intensity peak at around at 2θ of 30.6° (JCPDS#00-004 – 0673) and second highest at 36.36° (JCPDS#00-004 – 0686) correspond to Sn and Pb rich phases respectively. In the pristine Sn-Pb-Sb and OD-Sn-Pb-Sb alloy, the prominent Sn rich phase peaks show that surface of the electrode is rich in Sn whereas the XRD profile of OD-Sn-Pb-Sb after eCO_2R shows that Pb rich phase peak intensity has increased at the expense of Sn rich phase peaks. The XRD analysis, thus suggests that bulk crystal phase retains

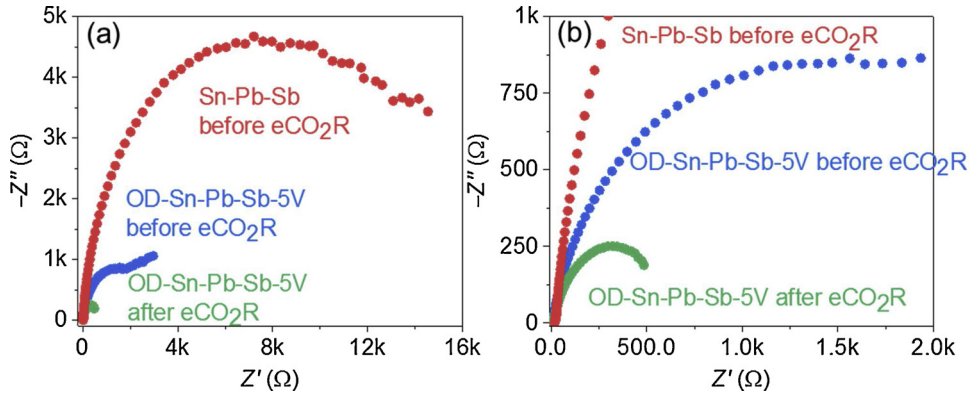

Fig. 7. (a) EIS spectra of pristine Sn-Pb-Sb and OD-Sn-Pb-S-5V and (b) enlarged spectra of the same; in CO_2 saturated 0.1 M $KHCO_3$ at open circuit potential.

similar structure in response to oxidation treatment of Sn-Pb-Sb alloy. However, during eCO_2R reaction, a compositional change in the alloy surface and bulk was observed which turned Sn rich structure to Pb rich structure. This suggests that during the eCO_2R reaction not only CO_2 was being reduced but surface restructuring was also occurring amongst multi-metals (Sn, Pb and Sb) as confirmed by EDX analysis as well.

SEM and EDX analysis were carried out and the surface morphology and composition of the OD-Sn-Pb-Sb-5 V alloy was analysed as shown in Fig. 10. Fig. 10 (a) shows the SEM image of pristine alloy before CO_2 reduction. The image shows that the alloy has two phases spread over homogenously. The light grey phase represents a Sn rich area while dark grey areas corresponds to Pb rich area. Sb is distributed homogenously on the Sn rich areas as confirmed by EDX mapping analysis in Fig. 10 (a). The alloy electrode shows the flat surface structure and that the average grain size is relatively large (~ 3 − 4 μm). The SEM image in Fig. 10 (b) shows the morphology of the electrode after eCO_2R exhibiting the surface restructuring. The two phase structure became less evident during eCO_2R process, although Sn, Pb and Sb rich and deficient areas are still distinguishable from EDX analysis (Fig. 10 (b)).

Fig. 11 shows OD-Sn-Pb-Sb-5 V electrode after eCO_2R. The electrode surface shows porous morphology with spherical particles distributed on the grain edges (inset image). The EDX mapping analysis shows that large grains are Pb rich areas while small particles are richer in Sn. The Sn and Sb are co-located while Pb rich areas are relatively segregated although Sn, Pb and Sb are presence could be seen all over the surface. The SEM and EDX mapping were carried out for OD-Sn-Pb-Sb-7 V as well and results are presented in Fig. SI 3) which confirms the similar observation for OD-Sn-Pb-Sb-5 V.

Although several material characterization techniques including SEM, EDX and CV analysis confirmed that Sn and Sn-Pb-Sb electrode surface were been modified under oxidation treatments nonetheless, it

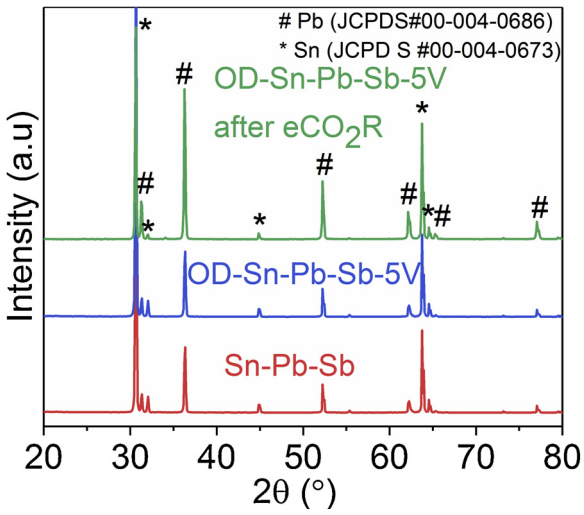

Fig. 9. XRD profiles of pristine, OD and OD-Sn-Pb-Sb-5V after eCO_2R.

is quite hard to establish the exact nature of the surface of the electrocatalysts from these techniques. Moreover, it is well known that the eCO_2R activity is a surface dependent phenomenon. Surface analysis techniques such as XPS need to be carried out. Thus to confirm the nature of surface composition and oxidation states of alloy electrodes XPS analysis was carried in detail as show in Figs. 12–14. Fig. 12 shows the XPS spectra of Sn 3*d* for a) Pristine Sn-Pb-Sb, (b) OD-Sn-Pb-Sb and (c) OD-Sn-Pb-Sb after eCO_2R. The 3*d* Sn spectrum of pristine Sn-Pb-Sb shows the presence of two oxidation states of Sn i.e. Sn metal at 485.0 eV and SnO_2 at 486.9 eV. The Sn $3d_{5/2}$ and Sn $3d_{3/2}$ peaks for both metal and oxide are separated by 8.4 eV. The XPS analyses suggest

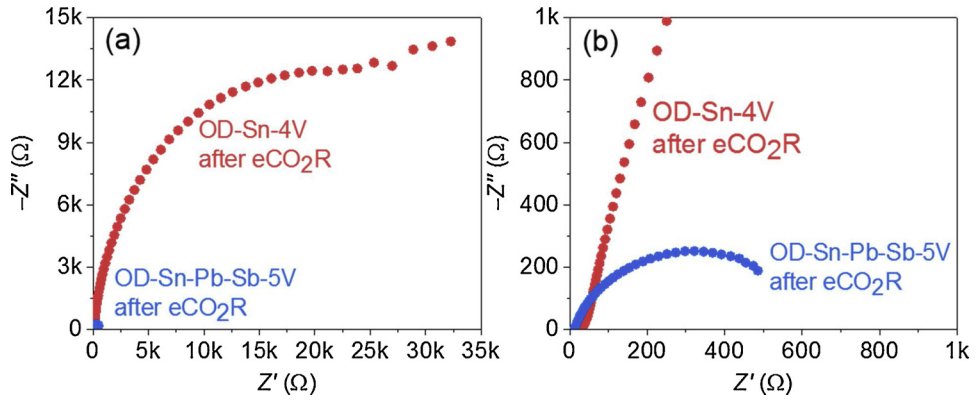

Fig. 8. (a) EIS spectra of OD-Sn-4 V and OD-Sn-Pb-S-5V after eCO_2R and (b) enlarged spectra of the same; in CO_2 saturated 0.1 M $KHCO_3$ at open circuit potential.

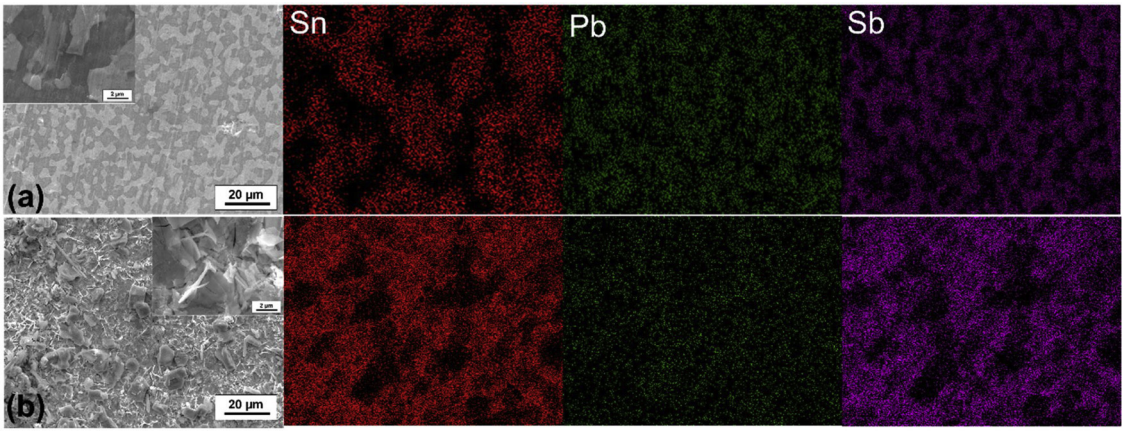

Fig. 10. SEM images and EDX mapping of Sn-Pb-Sb alloy electrode, (a) before (b) after CO_2 reduction.

that both Sn^0 and Sn^{4+} species exist on the surface of pristine Sn-Pb-Sb. Since the alloy was fabricated and stored in open atmosphere, the Sn oxide in pristine alloy may arise from atmospheric oxidation. Fig. 12 (b) shows the Sn 3*d* spectrum of OD-Sn-Pb-Sb-5 V electrode before eCO_2R. The spectrum shows that in OD-Sn-Pb-Sb-5 V alloy, the metallic Sn surface is completely oxidized to generate SnO_2 with no remaining metallic specie. The OD-Sn-Pb-Sb-5 V electrode was tested for eCO_2R afterwards and XPS spectrum of Sn 3*d* is shown in Fig. 12(c). The XPS spectrum shows that reappearance of two oxidation states of Sn i.e. Sn metal and SnO_2. The results confirm that SnO_2 species in OD-Sn-Pb-Sb-5 V alloy are partially reduced to generate Sn metal without reducing the entire oxide species. This brings to the conclusion that the change of OD-Sn-Pb-Sb surface composition during the eCO2R process may affect the CO_2 adsorption on the catalyst and causing the changes on activity of the catalyst during eCO_2R.

The XPS analysis of the OD-Sn-Pb-Sb-5 V was carried out on Pb 4*f* and the results are shown in Fig. 13 (a–c). The Pb $4f_{5/2}$ spectrum of pristine Sn-Pb-Sb displays two distinct states of Pb in the alloy i.e. Pb metal and PbO_2. Both of the Pb metal and PbO_2 spin-orbit components are well separated by 4.87 eV in Pb 4*f* region. Analysis of the O1 s region (Fig. 14) for air-exposed Pb metal indicates the native PbO_2 may have a high concentration of hydroxide. Moreover, PbO_2 may have a small amount of $PbCO_3$ formed on surface through reaction with CO_2 in the atmosphere. Additionally, Sn 4*s* overlaps the region with Pb 4*f* and was fitted accordingly. Fig. 13 (b) displays the Pb 4*f* spectrum of OD-Sn-Pb-Sb-5 V before eCO_2R. The spectrum indicates that pristine Sn-Pb-Sb surface has been mostly oxidized however, a small amount of metallic Pb is present even after oxidation treatment. The Pb 4f XPS spectrum of OD-Sn-Pb-Sb-5 V after eCO_2R is presented in Fig. 13 (c). The spectrum shows that the OD-Sn-Pb-Sb-5 V alloy has transformed after eCO_2R into three distinctive phases including Pb metal, PbO_2 and forming a new phase i.e. $PbCO_3$. $PbCO_3$ formation could be attributed to the reaction of PbO_2 with CO_2 during or after the reaction. The complete set of Pb 4*f* results confirm that the final state of the OD-Sn-Pb-Sb-5 V alloy electrocatalyst consists of composite Pb structure including Pb metal, PbO_2 and $PbCO_3$. Thus the enhanced eCO_2R performance of OD-Sn-Pb-Sb-5 V alloy could well be attributed to the composite structure of the alloy where PbO_2 and $PbCO_3$ may reinforce the CO_2 adsorption whereas Pb metal may assist in electron transfer.

XPS spectra of O 1*s* and Sb 3*d* are shown in Fig. 14 for (a) Pristine Sn-Pb-Sb, (b) OD-Sn-Pb-Sb and (c) OD-Sn-Pb-Sb after eCO_2R. The spectrum in Fig. 14 (a) shows that pristine Sn-Pb-Sb has metallic Sb $3d_{5/2}$ at 527.8 eV where the spectrum is mainly dominated by O1 s components arising from the metallic oxides other than Sb and presence of hydroxides. The fitted O 1*s* and Sb 3*d* for OD-Sn-Pb-Sb are shown in Fig. 14 (c) which endorses the complete conversion of metallic Sb into Sb_2O_5 at 530.5 eV along with presence of oxides and hydroxides. Moreover, Sb 3*d* region has well separated spin-orbit components between Sb 3 $d_{5/2}$ and Sb $d_{3/2}$ with 9.39 eV. Since, there is direct overlap between Sb $3d_{5/2}$ and O1*s* peaks, Sb $3d_{3/2}$ was used as a guide for peak fitting which does not overlap with O1 s. Moreover, the intensity and binding energy of Sb $3d_{5/2}$ peak was set by the Sb $3d_{3/2}$ peak, according to the spin-orbit splitting and ratio and remainder of intensity under at Sb $3d_{5/2}$ energy was attributed to oxygen. Similarly, Fig. 14. (c) shows the fitted O 1*s* and Sb 3*d* spectrum for OD-Sn-Pb-Sb-5 V after eCO_2R displaying two phases of Sb including Sb metal and Sb_2O_5 and O 1*s* spectra as discussed earlier. It is noteworthy that during the eCO2R, Sb_2O_5 is not completely reduced and final surface structure of the electrode consists of composite of Sb metal and Sb_2O_5.

3.3. Stability study of OD-Sn-Pb-Sb-5V electrode

To evaluate the stability of the electrocatalysts, eCO_2R was carried out at various controlled potentials in CO_2 saturated 0.1 M $KHCO_3$. The stability performance of the OD-Sn-Pb-Sb-5V electrode at – 1.4 and −1.2 V vs. RHE is demonstrated in Fig. 15. The reaction was intentionally stopped after 2 h and allowed to stand overnight (˜ 12 h) to observe the degradation of the electrode under open-circuit aqueous conditions. The reaction was then restarted for an additional 2 h. The results indicated that the OD-Sn-Pb-Sb-5V electrocatalyst is stable under aqueous eCO_2R conditions, with an 88% FE_{HCOO-} at −1.4 and 83% FE at −1.2 V vs. RHE for 4 h. The overall eCO_2R performance of the OD-Sn-Pb-Sb-5V commercial alloy is competitive with other recently reported Sn based alloys as shown in Table SI 1 [10,22–24].

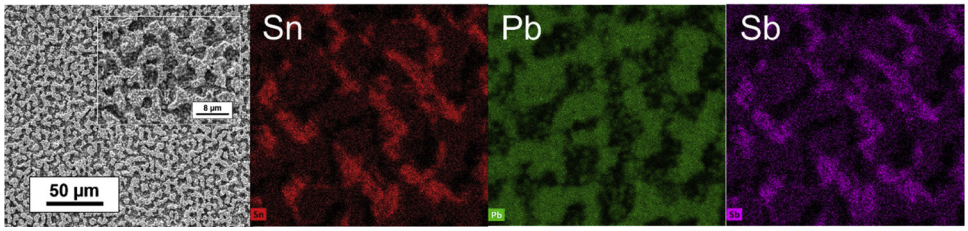

Fig. 11. SEM images and EDX mapping of oxidized Sn-Pb-Sb electrode at 5 V after CO_2R.

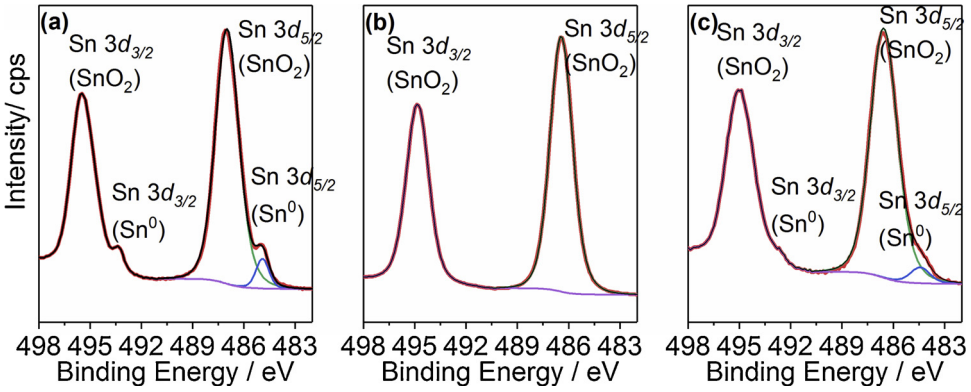

Fig. 12. XPS spectra of Sn 3*d* (a) Pristine Sn-Pb-Sb, (b) OD-Sn-Pb-Sb and (c) OD-Sn-Pb-Sb after eCO_2R.

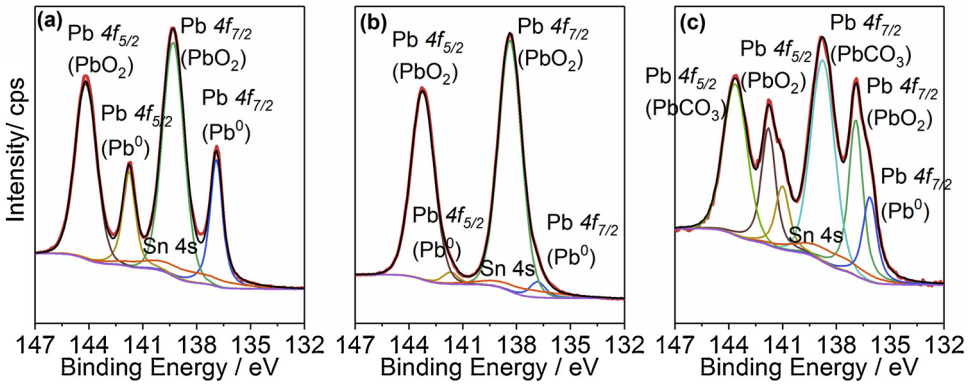

Fig. 13. XPS spectra of Pb 4*f* (a) Pristine Sn-Pb-Sb, (b) OD-Sn-Pb-Sb and (c) OD-Sn-Pb-Sb after eCO_2R.

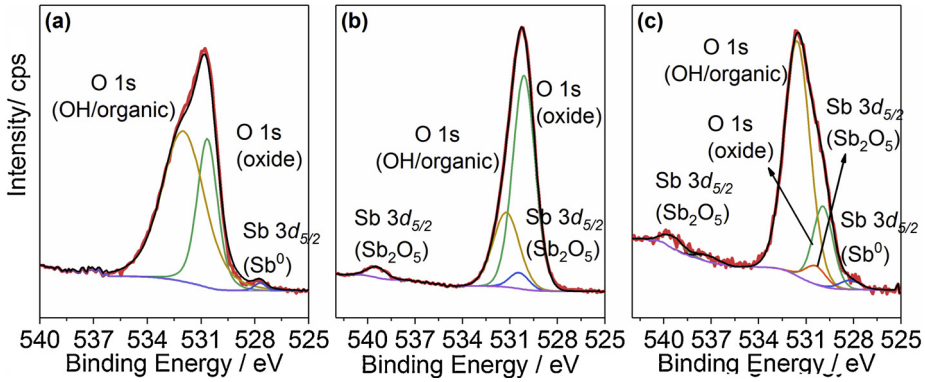

Fig. 14. XPS spectra of O 1*s* and Sb 3*d* (a) Pristine Sn-Pb-Sb, (b) OD-Sn-Pb-Sb and (c) OD-Sn-Pb-Sb after eCO_2R.

3.4. Comparison of eCO_2R performance of OD-Sn and OD-Sn-Pb-Sb catalysts

The eCO_2R performance of the OD-Sn-5 V and OD-Sn-Pb-Sb-5V alloy is summarized in Table 1. The eCO_2R performance of the OD-Sn-Pb-Sb alloy is distinctively higher than eCO_2R performance of OD-Sn electrodes at a range of applied potentials under similar experimental conditions. These results suggest that alloying may alter both the electronic and geometric structure of the catalytically active sites. The alteration of electronic structure of the alloy OD-Sn-Pb-Sb catalyst is directly related to intermediate binding ($CO^{-\cdot}$), which may influence the reaction pathway for formate production. Additionally, geometric structural changes due to oxidation treatment may affect the local atomic arrangement at the active site favouring the stability of $CO^{-\cdot}$ intermediates [11,34]. Thus, there is a consistent relationship between changing morphology and electronic effects in OD-Sn-Pb-Sb electrodes. The selectivity (FE_{HCOO-}) and activity (j / mA cm^{-2}) of the OD-Sn-Pb-Sb alloy is higher than the eCO_2R performance of pristine Sn-Pb-Sb as depicted in the schematic in Fig. 16.

We conclude following structure–property relationships from the eCO_2R activity of the alloy electrocatalysts:

1 Sn metal suppresses the H_2 production in favour of $HCOO^-$ production especially at higher overpotentials. This effect becomes even more pronounced when the OD-Sn electrodes are employed for eCO_2R (FE_{HCOO-} increases with OD electrodes at higher overpotentials).
2 The pristine Sn-Pb-Sb alloy consists of native oxides present on the surface. Even the presence of these native oxides produces less $HCOO^-$ than pristine Sn metal showing that only the synergistic electronic structure effects from multi-metals due to alloying may not be favourable to eCO_2R.

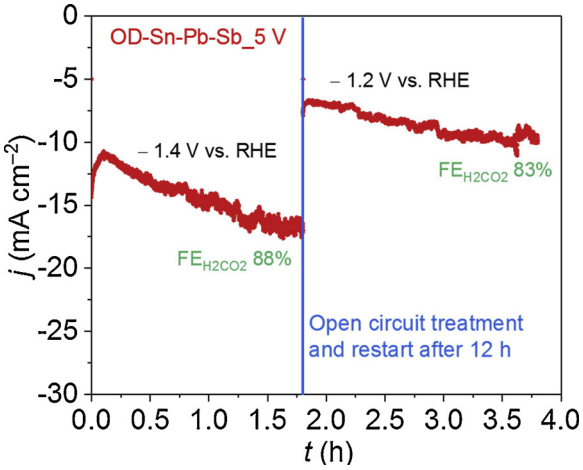

Fig. 15. The stability test for the OD-Sn-Pb-Sb-5V electrode in CO_2 saturated 0.1 M $KHCO_3$.

Table 1
Comparison of eCO_2R performance of an OD-Sn and OD-Sn-Pb-Sb electrodes in 0.1 M $KHCO_3/CO_2$ at different potentials.

Electrode	E (V vs. RHE)	j (mA cm^{-2})	FE (%)
OD-Sn-5 V	−1.4	5.6	74
	−1.2	4.1	77
	−1.0	3.5	36
OD-Sn-Pb-Sb-5 V	**−1.4**	**8.3**	**91**
	−1.2	6.0	83
	−1.0	2.9	58

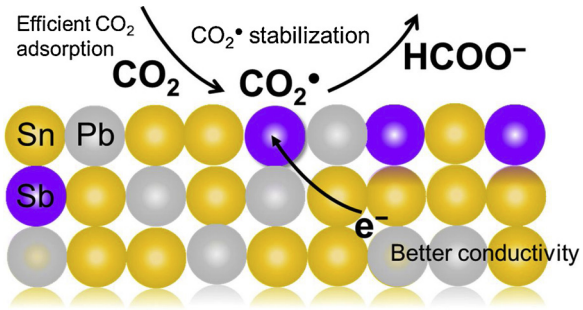

Fig. 16. Schematic showing eCO_2R on a Sn-Pb-Sb alloy electrodes.

3 Planned oxidation of Sn-Pb-Sb electrode to obtain OD-Sn-Pb-Sb electrocatalyst favours $HCOO^-$ formation compared to pristine Sn-Pb-Sb and even OD-Sn electrodes. The enhanced eCO_2R activity could be the result of metal/metal oxide composite structure where metal oxide is helping the better adsorption of CO_2 and stability of $CO^{-\cdot}$ whereas metal is helping the charge transfer reaction as shown in the schematic (Fig. 16). This means the synergistic underpinning from both the geometric and electronic effects is essential for better eCO_2R activity.

4 The role of Sb in the ternary Sn based alloy appears to be quite important and this result brings another interesting aspect regarding the utilization of SnO_2 based electrocatalysts for eCO_2R where SnO_2 could be doped with Sb like metals to improve the activity and selectivity of the electrocatalysts. Moreover, the formation of $PbCO_3$ on the surface of the Sn-Pb-Sb alloy may well improve the CO_2 adsorption mechanism which may pave a path towards better designing of the electrocatalysts for eCO_2R.

4. Conclusions

In this study, oxide-derived OD-Sn and commercially available OD-Sn-Pb-Sb alloy catalysts for eCO_2R to formate production were systematically probed. The results demonstrate that OD-Sn-Pb-Sb alloy electrodes stand out as efficient electrocatalysts for eCO_2R for formate production with good stability for 16 h. OD-Sn-4 V exhibited FE_{HCOO-} upto 84% at the expense of decreased current density upon oxidation treatment. On the contrary, FE_{HCOO-} for OD-Sn-Pb-Sb alloy improved remarkably to 91% without decrease in current density. The perseverance of the electrocatalytic activity of the OD Sn-Pb-Sb alloy electrocatalyst is attributed to the presence of Sb which improved the electronic conductivity of SnO_2. The superior eCO_2R activity of OD-Sn-Pb-Sb electrodes relative to the Sn-Pb-Sb alloy electrodes could be attributed to metal/metal oxide composite structure arising from the synergistic geometric and electronic effects of the multi-metallic centres. The higher eCO_2R performance of low cost OD-Sn-Pb-Sb multi-metallic alloy suggest that these alloys could be employed commercially and may pave a path for scalable eCO_2R systems.

Acknowledgements

The authors thank EPSRC LifesCO2R project (EP/N009746/1), EPSRC NECEM (EP/R021503/1) and NERC MeteoRR (NE/L014246/1). Hang Xiang thanks the Doctor Training Awards (SAgE DTA, 2015 cohort). XPS data collection was performed at the EPSRC National Facility for XPS (‘HarwellXPS’), operated by Cardiff University and UCL, under contract No. PR16195. The authors thank Maggie White for XRD measurement, and Dr. Isabel Garcia for SEM/EDX analysis.

Appendix A. Supplementary data

Supplementary material related to this article can be found, in the online version, at doi:https://doi.org/10.1016/j.jcou.2019.03.016.

References

[1] F. Studt, I. Sharafutdinov, F. Abild-Pedersen, C.F. Elkjær, J.S. Hummelshøj, S. Dahl, I. Chorkendorff, J.K. Nørskov, Discovery of a Ni-Ga catalyst for carbon dioxide reduction to methanol, Nat. Chem. 6 (2014) 320–324.
[2] Y. Hori, H. Wakebe, T. Tsukamoto, O. Koga, Electrocatalytic process of CO selectivity in electrochemical reduction of CO2 at metal electrodes in aqueous media, Electrochim. Acta 39 (1994) 1833–1839.
[3] J. Wu, F. Risalvato, X.-D. Zhou, Effects of the electrolyte on electrochemical reduction of CO2 on Sn electrode, ECS Trans. 41 (2012) 49–60.
[4] T. Hatsukade, K.P. Kuhl, E.R. Cave, D.N. Abram, T.F. Jaramillo, Insights into the electrocatalytic reduction of CO2 on metallic silver surfaces, PCCP 16 (2014) 13814–13819.
[5] J.T. Feaster, C. Shi, E.R. Cave, T. Hatsukade, D.N. Abram, K.P. Kuhl, C. Hahn, J.K. Nørskov, T.F. Jaramillo, Understanding selectivity for the electrochemical reduction of carbon dioxide to formic acid and carbon monoxide on metal electrodes, ACS Catal. 7 (2017) 4822–4827.
[6] Y. Hori, Electrochemical CO2 reduction on metal electrodes, in: C. Vayenas (Ed.), Modern Aspects of Electrochemistry, Springer, New York, 2008.
[7] G.O. Larrazábal, A.J. Martín, F. Krumeich, R. Hauert, J. Pérez-Ramírez, Solvothermally-prepared Cu2O electrocatalysts for CO2 reduction with tunable selectivity by the introduction of p-Block elements, ChemSusChem 10 (2017) 1255–1265.
[8] Y. Chen, M.W. Kanan, Tin oxide dependence of the CO2 reduction efficiency on tin electrodes and enhanced activity for Tin/Tin oxide thin-film catalysts, J. Am. Chem. Soc. 134 (2012) 1986–1989.
[9] Q. Li, J. Fu, W. Zhu, Z. Chen, B. Shen, L. Wu, Z. Xi, T. Wang, G. Lu, J.-j. Zhu, S. Sun, Tuning Sn-Catalysis for electrochemical reduction of CO2 to CO via the Core/Shell Cu/SnO2 structure, J. Am. Chem. Soc. 139 (2017) 4290–4293.
[10] W. Luc, C. Collins, S. Wang, H. Xin, K. He, Y. Kang, F. Jiao, Ag–Sn bimetallic catalyst with a core–Shell structure for CO2 reduction, J. Am. Chem. Soc. 139 (2017) 1885–1893.
[11] J. He, N.J.J. Johnson, A. Huang, C.P. Berlinguette, Electrocatalytic alloys for CO2 reduction, ChemSusChem 11 (2018) 48–57.
[12] L. Yanan, Q. Jinli, Z. Xia, L. Tao, G. Abel, L. Yuyu, Z. Jiujun, Rational design and synthesis of SnOx electrocatalysts with coralline structure for highly improved aqueous CO2 reduction to formate, ChemElectroChem 3 (2016) 1618–1628.
[13] S. Rasul, A. Pugnant, E. Yu, Electrochemical reduction of CO2 at multi-metallic interfaces, 233rd ECS MEETING, ECS (2018).

[14] M. Azuma, K. Hashimoto, M. Hiramoto, M. Watanabe, T. Sakata, Electrochemical reduction of carbon dioxide on various metal electrodes in low-temperature aqueous KHCO 3 media, J. Electrochem. Soc. 137 (1990) 1772–1778.
[15] Z.M. Detweiler, J.L. White, S.L. Bernasek, A.B. Bocarsly, Anodized indium metal electrodes for enhanced carbon dioxide reduction in aqueous electrolyte, Langmuir 30 (2014) 7593–7600.
[16] J. Guo, S. Ouyang, T. Kako, J. Ye, Mesoporous In(OH)3 for photoreduction of CO2 into renewable hydrocarbon fuels, Appl. Surf. Sci. 280 (2013) 418–423.
[17] C.W. Li, M.W. Kanan, CO2 reduction at Low Overpotential on Cu electrodes resulting from the reduction of thick Cu2O films, J. Am. Chem. Soc. 134 (2012) 7231–7234.
[18] Y. Chen, C.W. Li, M.W. Kanan, Aqueous CO2 reduction at very low overpotential on oxide-derived Au nanoparticles, J. Am. Chem. Soc. 134 (2012) 19969–19972.
[19] J. Qiao, Y. Liu, F. Hong, J. Zhang, A review of catalysts for the electroreduction of carbon dioxide to produce low-carbon fuels, Chem. Soc. Rev. 43 (2014) 631–675.
[20] C. Roy, J. Galipaud, L. Fréchette-Viens, S. Garbarino, J. Qiao, D. Guay, CO2 electroreduction at AuxCu1-x obtained by pulsed laser deposition in O2 atmosphere, Electrochim. Acta 246 (2017) 115–122.
[21] X. Zhang, T. Lei, Y. Liu, J. Qiao, Enhancing CO2 electrolysis to formate on facilely synthesized Bi catalysts at low overpotential, Appl. Catal. B Environ. 218 (2017) 46–50.
[22] S.Y. Choi, S.K. Jeong, H.J. Kim, I.-H. Baek, K.T. Park, Electrochemical reduction of Carbon Dioxide to formate on tin–Lead alloys, ACS Sustain. Chem. Eng. 4 (2016) 1311–1318.
[23] Q. Lai, N. Yang, G. Yuan, Highly efficient In–Sn alloy catalysts for electrochemical reduction of CO2 to formate, Electrochem. Commun. 83 (2017) 24–27.
[24] W.J. Dong, C.J. Yoo, J.-L. Lee, Monolithic nanoporous in–Sn alloy for electrochemical reduction of carbon dioxide, ACS Appl. Mater. Interfaces 9 (2017) 43575–43582.
[25] G.O. Larrazábal, A.J. Martín, J. Pérez-Ramírez, Building blocks for high performance in electrocatalytic CO2 reduction: materials, optimization strategies, and device engineering, J. Phys. Chem. Lett. 8 (2017) 3933–3944.
[26] J. He, K.E. Dettelbach, A. Huang, C.P. Berlinguette, Brass and Bronze as Effective CO2 Reduction Electrocatalysts, Angewandte Chemie International Edition 56 (52) (2017) 16579–16582.
[27] S. Rasul, D.H. Anjum, A. Jedidi, Y. Minenkov, L. Cavallo, K. Takanabe, A highly selective copper–Indium bimetallic electrocatalyst for the electrochemical reduction of aqueous CO2 to CO, Angew. Chem. 127 (2015) 2174–2178.
[28] A. Jedidi, S. Rasul, D. Masih, L. Cavallo, K. Takanabe, Generation of Cu-In alloy surfaces from CuInO2 as selective catalytic sites for CO2 electroreduction, J. Mater. Chem. A 3 (2015) 19085–19092.
[29] S. Sarfraz, A.T. Garcia-Esparza, A. Jedidi, L. Cavallo, K. Takanabe, Cu–Sn bimetallic catalyst for selective aqueous electroreduction of CO2 to CO, ACS Catal. 6 (2016) 2842–2851.
[30] C.W. Li, J. Ciston, M.W. Kanan, Electroreduction of carbon monoxide to liquid fuel on oxide-derived nanocrystalline copper, Nature 508 (2014) 504–507.
[31] S. Nakayama, T. Sugihara, J. Matsumoto, T. Notoya, T. Osakai, Chemical state analysis of tin oxide films by voltammetric reduction, J. Electrochem. Soc. 158 (2011) C341–C345.
[32] A. Palacios-Padrós, F. Caballero-Briones, I. Díez-Pérez, F. Sanz, Tin passivation in alkaline media: formation of SnO microcrystals as hydroxyl etching product, Electrochim. Acta 111 (2013) 837–845.
[33] B. Orel, U. Lavrenčič-Štangar, K. Kalcher, Electrochemical and structural properties of SnO2 and Sb : SnO2 transparent electrodes with mixed electronically conductive and ion-storage characteristics, J. Electrochem. Soc. 141 (1994) L127–L130.
[34] D. Childers, An Exploration of Geometric and Electronic Effects in Metal Nanoparticle Catalysts, Chemical Engineering, University of Illinois, Chicago, 2014.